Energy Frontier Research Center for Solid-State Lighting Science: Exploring New Materials Architectures and Light Emission Phenomena

Citation	Coltrin, M. E., Armstrong, A. M., Brener, I., Chow, W. W., Crawford, M. H., Fischer, A. J., ... & Wright, J. B. (2014). Energy Frontier Research Center for Solid-State Lighting Science: Exploring New Materials Architectures and Light Emission Phenomena. Journal of Physical Chemistry C, 118(25), 13330-13345. doi:10.1021/jp501136j
DOI	10.1021/jp501136j
Publisher	American Chemical Society
Version	Version of Record
Terms of Use	http://cdss.library.oregonstate.edu/sa-termsofuse

THE JOURNAL OF PHYSICAL CHEMISTRY C

Feature Article

pubs.acs.org/JPCC

Energy Frontier Research Center for Solid-State Lighting Science: Exploring New Materials Architectures and Light Emission Phenomena

Michael E. Coltrin,*[,†] Andrew M. Armstrong,[†] Igal Brener,[†] Weng W. Chow,[†] Mary H. Crawford,[†] Arthur J. Fischer,[†] David F. Kelley,[‡] Daniel D. Koleske,[†] Lincoln J. Lauhon,[§] James E. Martin,[†] May Nyman,[∥] E. Fred Schubert,[⊥] Lauren E. Shea-Rohwer,[†] Ganapathi Subramania,[†] Jeffrey Y. Tsao,[†] George T. Wang,[†] Jonathan J. Wierer, Jr.,[†] and Jeremy B. Wright[†]

[†]Sandia National Laboratories, P.O. Box 5800, MS-1086, Albuquerque, New Mexico 87185-1086, United States

[‡]Chemistry and Chemical Biology, University of California Merced, Merced, California 95343, United States

[§]Department of Materials Science and Engineering, Northwestern University, Evanston, Illinois 60208, United States

[∥]Department of Chemistry, Oregon State University, Corvallis, Oregon 87331, United States

[⊥]Department of Electrical, Computer and Systems Engineering, Rensselaer Polytechnic Institute, Troy, New York 12180, United States

ABSTRACT: The Energy Frontier Research Center (EFRC) for Solid-State Lighting Science (SSLS) is one of 46 EFRCs initiated in 2009 to conduct basic and use-inspired research relevant to energy technologies. The overarching theme of the SSLS EFRC is the exploration of energy conversion in tailored photonic structures. In this article we review highlights from the research of the SSLS EFRC. Major research themes include: studies of the materials properties and emission characteristics of III-nitride semiconductor nanowires; development of new phosphors and II−VI quantum dots for use as wavelength downconverters; fundamental understanding of competing radiative and nonradiative processes in current-generation, planar light-emitting diode architectures; understanding of the electrical, optical, and structural properties of defects in InGaN materials and heterostructures; exploring ways to enhance spontaneous emission through modification of the environment in which the emission takes place; and investigating routes such as stimulated emission that might outcompete nonradiative processes.

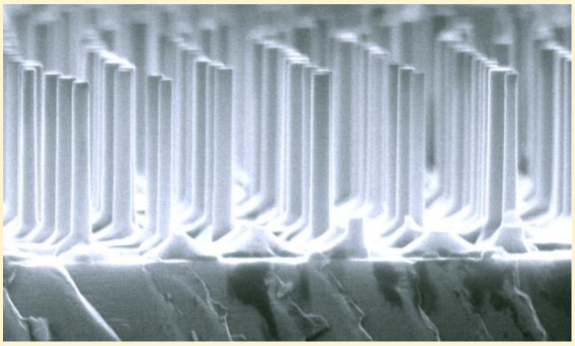

INTRODUCTION

Artificial light has long been a significant factor contributing to the quality and productivity of human life.[1] As a consequence, human civilization uses huge amounts of energy to produce it. Today, artificial light consumes an estimated 0.72% of world GDP and, due to its high energy intensity, an estimated 6.5% of world primary energy and 16% of world electrical energy.[1]

Solid-state lighting is an emerging technology in which solid-state devices, like light-emitting diodes (LEDs) or laser diodes (LDs), are used to produce artificial light for general illumination. Solid-state lighting (SSL) efficiencies have increased steadily over the past decade and are now greater than those of incandescent and fluorescent lamps.[2] However, commercial SSL is still only ∼25% efficient, and there is thus much room for further improvement.

To help lay the scientific foundations for that improvement, the Energy Frontier Research Center (EFRC) for Solid-State Lighting Science (SSLS) was one of 46 EFRCs initiated in 2009 to conduct basic and use-inspired research relevant to energy technologies. The overarching theme of this center is "exploring energy conversion in tailored photonic structures", and in this article we review highlights from the research of the SSLS EFRC.

Figure 1 presents a sketch of a common state-of-the-art commercial white solid-state lamp, along with the spectral power density of its emission. The lamp consists of a blue LED, 1-square-mm in size, driven with 0.7 A of current, and coated with green and red phosphors.[3] Some of the blue light from the LED leaks through the phosphors, giving the relatively narrow blue peak in the spectral power density. However, some blue light is absorbed by the phosphors and is re-emitted as green and red light, giving the two relatively wide green and red peaks in the spectral power density. The combination of blue, green, and red light is both pleasing to the human eye and faithfully renders colors of viewed objects. The lamp's ∼25% efficiency is due to the cumulative effect of three subefficiencies,[4] with the

Received: January 31, 2014
Revised: April 8, 2014
Published: April 22, 2014

   dx.doi.org/10.1021/jp501136j | J. Phys. Chem. C 2014, 118, 13330−13345

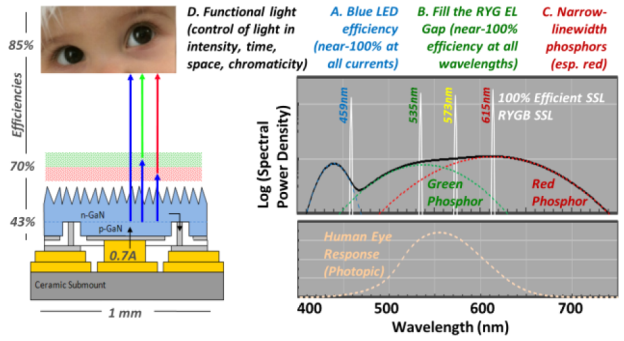

Figure 1. Sketch of a common state-of-the-art commercial white solid-state lamp, along with its emission spectral power density. (With permission of John Wiley & Sons, Inc.; photo credit http://bobbymercerbooks.com/).

contribution of each subefficiency identifiable with a particular SSL technology challenge (A–C in Figure 1).

The first subefficiency is that of the blue LED, which is currently ~43% at a current density of ~700 mA into a mm^2 chip for the illustrated device. This is much lower than the best thus-far-reported lab result, 81%, for a much lower current density[5] (25 mA/mm^2), due to an "efficiency droop"—a decrease in efficiency with increased injected-current density, which is the subject of intense research interest.[6] We use here the subefficiency at the higher current density because higher current densities (at least 700 mA and ideally 2 A into a mm^2 chip) are desirable to defray the manufacturing cost of the SSL chip. So a first SSL technology challenge (A in Figure 1) is to increase blue LED efficiency, particularly at high current densities.

The second subefficiency, that of the phosphors and package, is about 70%. Some of this is because the phosphors do not have perfect quantum yield; that is, one blue photon in does not result in one red or green photon out. However, quantum yields are improving, leaving a more fundamental efficiency loss, the so-called Stokes deficit, which is the quantum energy deficit associated with converting a blue into a red or green photon. One way of eliminating this loss would be to eliminate phosphors altogether through use of direct electroluminescent (EL) emitters. However, the current state-of-the-art visible electroluminescent semiconductors, InGaN and InGaAlP, have low efficiencies in the red–yellow–green spectral range necessary for high-color-quality white light. Thus, a second SSL technology challenge (B in Figure 1) is to fill the red–yellow–green (RYG) gap in semiconductor electroluminescence.

The third subefficiency is associated with the match between the spectrum of emitted white light and the human eye sensitivity and is of the order ~85%. The red phosphor (dashed red curve in Figure 1) used in the white lamp is centered at a wavelength of 615 nm, which is the ideal peak emission wavelength at the red end of the spectrum to provide good color rendering. However, current phosphors also emit quite far into the deep red—so deep that the human eye is not very sensitive to it, as can be seen from the human eye response (dashed pink curve in Figure 1). This spillover into the deep red due to the broad phosphor emission accounts for the loss in "efficiency" due to the LED emission spectrum.[7,8] So, a third SSL technology challenge (C in Figure 1) is to find an efficient narrow-line-width red wavelength downconverter.

Note that there is one subefficiency that does not enter into the overall ~25% lamp efficiency but that we mention here for completeness: the subefficiency associated with the intelligent matching of light to its use. By intelligence we mean control of the artificial light so that it is on only *when* it is being used and is directed only *where* it is needed.[9] And, when and where it is being used, the intensity, chromaticity, and perhaps even the color rendering quality and luminous efficacy of the artificial light could all potentially be optimized to how it is being used. So a fourth SSL technology challenge (D in Figure 1) is creating light with this kind of intelligence.

OVERVIEW OF RESEARCH CHALLENGES: MATERIALS ARCHITECTURES AND LIGHT-EMISSION PHENOMENA

Although the three subefficiencies may not seem unacceptably low (43%, 70%, and 85%), due to their serial nature, their multiplicative effect is a net overall efficiency around 25%. Overcoming the three SSL technology challenges is thus extremely important. The goal of the SSLS EFRC is 2-fold: (a) to gain a deeper understanding of the materials architectures and light-emission phenomena used in current-day SSL approaches and (b) to explore new materials architectures and light-emission phenomena that have the potential for breakthroughs in energy efficiency. To do this, the SSLS EFRC is organized around six Research Challenges. As illustrated in Figure 2, two of the Research Challenges are focused on materials architectures, and four of the Research Challenges are focused on light-emission phenomena.

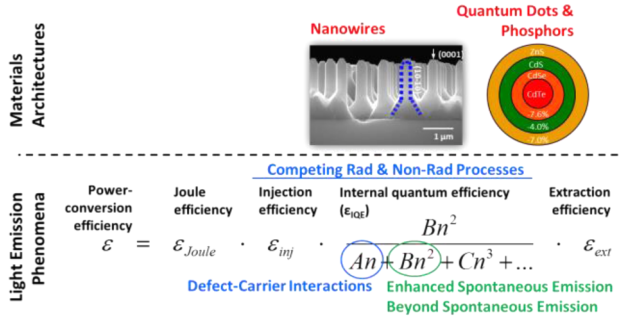

Figure 2. Schematic of the SSLS EFRC's six Research Challenges. The two at the top are focused on materials architectures, and the four at the bottom are focused on light-emission phenomena.

The two materials architecture Research Challenges are illustrated at the top of Figure 2, the first of which is the "Nanowires" Research Challenge. Because of their narrow diameters, nanowires have the potential to be fabricated without line defects and can accommodate more strain and therefore a wider range of compositions, including those that might enable high-efficiency green, yellow, and red light emission. The second materials architecture Research Challenge is "Quantum Dots and Phosphors," with applications to wavelength downconversion, particularly for narrow-line-width red emission.

The four light-emission phenomena Research Challenges are illustrated at the bottom of Figure 2. To put these four in context, Figure 2 shows the equation that parses out the various contributions to power-conversion efficiency of a light-emitting device. There is a Joule efficiency associated with resistive losses as carriers are transported from electrical contacts to the active

dx.doi.org/10.1021/jp501136j | J. Phys. Chem. C 2014, 118, 13330–13345

region of the device. Then there is an injection efficiency associated with whether, once the carriers get to the active region, they overshoot it or thermalize in it or if they do thermalize in it they then for whatever reason escape. Then there is an internal quantum efficiency associated with the fraction carriers that recombine radiatively (the spontaneous emission Bn^2 term, where n is carrier density) rather than nonradiatively (the defect-mediated An and Auger recombination Cn^3 terms). Finally, there is the extraction efficiency—the fraction of photons that are created in the device that escape.

The first two light-emission phenomena Research Challenges (in blue) focus on these various competing processes: "Competing Radiative and Nonradiative Processes" , examines the overall competition between the processes; "Defect–Carrier Interactions" examines one of the most important and fundamental of the processes, defect-mediated carrier recombination.

The second two light-emission phenomena Research Challenges (in green) focus on ways to alter internal quantum efficiency to better compete with parasitic nonradiative carrier recombination: "Enhanced Spontaneous Emission" explores ways of enhancing spontaneous emission through modification of the environment within which the emission takes place; "Beyond Spontaneous Emission" explores the possibility of going beyond spontaneous emission, through the addition of cavities and coherent processes, such as lasing.

MATERIALS ARCHITECTURES: NANOWIRES

Our "Nanowires" Research Challenge explores the synthesis and properties of GaN/InGaN nanowires (NWs) as a new materials architecture for visible-light emission. Among the many advantages of GaN/InGaN nanowires over presently employed planar GaN/InGaN films are the potential for high-quality material, without detrimental line defects; the ability to accommodate lattice strain and therefore a wider range of alloy compositions and bandgaps; manipulability of growth geometries to expose surface orientations with tailored light-emission properties and reduced piezoelectric fields; the large sidewall surface area available for active light emission; and the ability to create novel mesoscale structures such as photonic crystals. If nanowire light emitters could span the entire visible spectrum, the RYG-gap technology challenge would be overcome. In addition, full-spectrum emission would enable chromaticity tunability for intelligent lighting.[9] Table 1 summarizes the unique properties of nanowires and their potential benefit for lighting. The advantages of semiconductor nanowires for photonics[10] and GaN-based nanowires for lighting have been previously reviewed in detail.[11]

That said, application of GaN/InGaN nanowires for SSL is a relatively immature area of research. Thus, this Research Challenge is broad in scope, encompassing materials synthesis and processing of photo- and electroluminescent nanowires, including both axial and radial types, along with optical, electrical, mechanical, and structural characterization and modeling.

Table 1. Summary of Nanowire Properties and Potential Benefits for Lighting

nanowire property	benefit for SSL
strain accommodation	high In-content structures
	reduced dislocation densities
	growth on lattice mismatched substrates
high surface/device area	greatly increased areal device density
nonpolar sidewall facets	eliminate quantum confined Stark effect
2D arrangements possible	photonic crystals for light extraction
freestanding optical cavity	compact, low-power nanolasers possible

Bottom-Up and Top-Down Synthesis Methods. GaN-based nanowires are typically synthesized through bottom-up methods, including vapor–liquid–solid (VLS)[12,13] and catalyst-free selective-area growth (SAG).[14] Our early work was along these lines: Ni-catalyzed metalorganic chemical vapor deposition (MOCVD)[15,16] was used to synthesize vertically aligned GaN nanowires on $(1\bar{1}12)$ r-plane sapphire wafers.[17] Transmission electron microscopy (TEM) studies showed that these nanowires were single crystalline and oriented along the $[11\bar{2}0]$ direction, with isosceles triangular cross sections having two equivalent $\{\bar{1}101\}$ facets and one N-polar $(000\bar{1})$ c-plane facet. Promisingly, the nanowires were observed to be free of threading dislocations, though c-plane stacking faults were seen.

Bottom-up methods, however, particularly for GaN-based nanowires, require highly specific conditions, such as low V-to-III ratio, to promote anisotropic one-dimensional crystal growth. These growth conditions can potentially lead to lower overall crystal quality, the introduction of higher impurity and point defect densities, and less flexibility for adjusting growth conditions to control doping and composition.

Thus, our more recent work has explored complementary top-down methods. In particular, a new two-step top-down nanowire fabrication approach was developed that enables the formation of high-quality nanowire arrays with independently controlled pitch, height, and diameter,[18,19] as shown in Figure 3. The first step of the process is an anisotropic plasma etch of a c-plane GaN-based film through a self-assembled mask of monodisperse silica spheres (lithographically defined etch masks can also be used) to define tapered c-axis-oriented GaN pillars. The second step of the process is a facet-selective wet etch (using AZ400K photoresist developer) that removes the plasma-etch damage and results in nanowires with straight and smooth sidewalls and with diameters controlled by the wet etch time. A general comparison of GaN-based bottom-up and top-down fabricated nanowires, highlighting relative advantages and disadvantages of each method, is provided in Table 2.

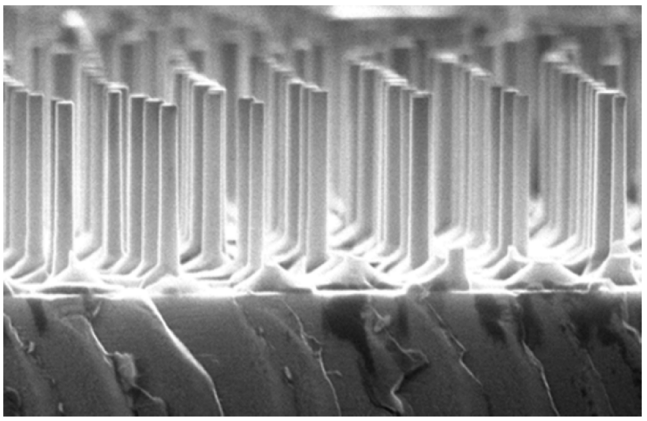

Figure 3. Array of GaN nanowires fabricated by a two-step dry plus wet top-down etching process.

In the remainder of this section we discuss some of the highlights of our work on GaN and InGaN nanowire structures

dx.doi.org/10.1021/jp501136j | J. Phys. Chem. C 2014, 118, 13330–13345

Table 2. Comparisons between Bottom-Up and Top-Down Methods for Fabricating GaN-Based Nanowires

	bottom-up	top-down
length	practically limited by growth rate	limited by starting material thickness and etch-mask selectivity
radial architectures?	by MOCVD	by MOCVD regrowth
axial architectures?	by MBE	yes
high In-content structures possible?	axial, yes; radial, potentially	radial, potentially by regrowth
characterization	some properties difficult to measure (e.g., doping)	pre-etched starting material measurable by standard techniques
dislocations	few to none	depends on film quality; can be largely dislocation free
material quality	point defect density may be high due to anisotropic growth conditions	starting material can be grown under optimal growth conditions
uniformity	wire-to-wire variations in size and properties; SAG may help	generally good, especially height

synthesized through various combinations of bottom-up and top-down methods.

Minority (Hole) Carrier Diffusion Length. Light-emitting devices often rely on transport of minority carriers in a background of majority carriers. In the ideal case, the minority carrier diffusion length is determined by a competition between the rate at which the minority carriers diffuse and the rate at which they recombine radiatively. In less ideal cases minority carriers can recombine nonradiatively at defects or surfaces, thus shortening the diffusion length. In nanowires, for which surfaces are nearby, this could be a major issue.

To understand this basic issue, we studied hole minority carrier diffusion lengths in GaN, GaN/AlGaN, and GaN/InGaN core−shell NWs grown by a two-step process: Ni-catalyzed axial MOCVD of a GaN core followed by radial MOCVD of an AlGaN or InGaN shell. The experiment made use of scanning electron microscopy to generate charge at a particular position on the nanowire, combined with near-field scanning optical microscopy to observe the spatial profile of the luminescence away from the charge-generation position.

The results were that, for GaN or GaN/InGaN nanowires, minority carrier diffusion lengths were indeed shorter than what would be expected for bulk GaN, likely due to surface recombination. For GaN/AlGaN nanowires, however, minority carrier diffusion lengths were in the 1 μm range, on the order of that expected for bulk GaN, consistent with the AlGaN shell acting as a higher-bandgap carrier confinement layer for holes in the GaN core.[20]

Mechanical Resilience. Ideally, solid-state light emitters are driven "hard" to maximize lumen output per chip and to minimize chip cost per lumen. Nanowire emitters for solid-state lighting might also be driven hard and hence be subject to mechanical stresses due to thermal gradients or thermal expansion mismatches in complex compositionally tailored structures. Moreover, new micro-opto-electromechanical (MOEM) functionalities that make use of strong piezoelectric effects in GaN-based materials might also lead to significant mechanical stresses.

To understand the response of nanowires to mechanical stress, we studied the deformation, fracture mechanisms, and fracture strength of individual GaN NWs grown by Ni-catalyzed MOCVD. The measurements were made in a unique transmission electron microscope−scanning probe microscope (TEM−SPM) platform that enabled high-resolution real-time imaging during deformation by a nanoscale "punch".[21]

One important result was that GaN NWs were resistant to plastic deformation by dislocation nucleation and propagation nearly up to the point of fracture, and even near the point of fracture, the lack of dislocation mobility in GaN caused dislocations to pile-up in, and plastic deformation to be localized to, the material just underneath the punch. This behavior is in strong contrast to that of metal NWs, in which dislocations propagate easily and enable global, not just local, plastic deformation.[22−27]

A second important result was that the fracture strength of the NWs increased sharply with decreasing NW diameter: in the 0.2 GPa range for 700 nm diameters to the 1.7 GPa range for 200 nm diameters. This result is curious and would be interesting to study further but suggests that GaN NWs will be mechanically resilient in many applications, and the more so the smaller their diameter.

Nanoscopically Nonuniform InGaN Shell Compositions. In many interesting nanowire configurations InGaN epitaxy on a nanostructure with anisotropic, faceted features might be required. The different facets and their intersections might have differing chemistries and nanoscopic local strains, differing In-to-Ga incorporation rates, and thus differing nanoscopic local InGaN alloy compositions.

To explore this possible phenomenon, InGaN coaxial shells were epitaxially grown on dislocation-free *a*-axis oriented GaN NWs, these NWs themselves grown via Ni-catalyzed MOCVD. The resulting nanoscopic local optical properties, indium concentrations, defect microstructures, and strain distributions of the InGaN shells were investigated using a combination of spatially resolved cathodoluminescence (CL), scanning transmission electron microscopy (STEM), and finite element computational analysis.[28]

The results were that for InGaN epitaxy on the semipolar $\{\bar{1}101\}$ facets 40% or greater indium compositions could be obtained, with luminescence observed into the near-infrared wavelengths. Dislocations were observed, in the 10^8 cm^{-2} range but at a much lower density than usually associated with the highly lattice-mismatched epitaxy of similar indium compositions on planar GaN surfaces.[29]

Indium was found to preferentially incorporate at the edge intersections (corners) between nanowire facets, where finite element analysis indicates strain was favorably tensile, rather than on the nanowire facets themselves, where finite element analysis indicates strain was unfavorably compressive. This is consistent with microscopic "lattice latching" or "compositional pulling", in which epitaxial growth favors compositions which minimize local strain energy.[30]

Note that, in some architectures, such nonuniform and anisotropic InGaN compositions might be disadvantageous. However, in some architectures (e.g., where quantum-scale InGaN features on a larger nanoscale structure are desired[31])

dx.doi.org/10.1021/jp501136j | J. Phys. Chem. C 2014, 118, 13330−13345

they might be advantageously utilized to tailor electron or optical confinement.

Axial NW LEDs. Top-down fabrication provides a route to axially heterostructured NW LEDs that are etched from a planar LED structure.[32] Such nanostructures might be expected to differ in performance from their planar parents in both positive and negative ways.

To explore these differences in performance, photoluminescence studies were performed on side-by-side samples of (a) vertically aligned, axial heterostructured InGaN/GaN nanowire LED arrays and (b) their parent planar LEDs. The InGaN/GaN multiple quantum well (MQW) active regions were along the nanowire axis and were created by "dry plus wet etching" (as discussed above) from "reasonable" quality planar LED structures, with peak internal quantum efficiency (IQE) ~ 27%.[19]

One first important result was a peak IQE (~24%) comparable to that (~27%) of the parent planar LED. Of course, this comparability could be the coincidental cancellation of a number of competing factors. On the one hand, e.g., nonradiative carrier recombination at dislocations might be reduced, as dislocation statistics (based on NW diameters and known parent material dislocation density and confirmed by TEM imaging) suggest that 94% of the nanowire LEDs are dislocation free. On the other hand, e.g., nonradiative carrier recombination might be enhanced at nearby surfaces and by heating due to poorer thermal conduction within the thin NW to the substrate. It will be of interest to study this more carefully in axial NWs etched from state-of-the-art (near-100% IQE) parent LEDs, in NWs with shell passivation, and under pulsed (no heating) conditions.

A second important result was a reduced quantum-confined Stark effect due to reduced piezoelectric fields caused by partial lateral strain relaxation of the quantum wells following etching of the planar LED into nanowires. This reduced quantum-confined Stark effect manifests itself as (a) a smaller red shift relative to the planar parent LED at low photopump intensity and (b) a much reduced blue shift relative to the planar parent LED with increasing photopump intensity due to free-carrier screening.

Our conclusion is that axial multiple-quantum-well NW LEDs have potential for SSL use and as nanoscale photonic elements. Even without special device designs to compensate for obvious disadvantages such as nonradiative carrier recombination at surfaces, peak IQEs are comparable to their parent LEDs, and quantum-confined Stark effects are much reduced.

Core/Shell NW LEDs and Solar Cells. We have also studied core/shell nanowire structures in which coaxial quantum-well/quantum-barrier multishells have been grown around a top-down etched GaN nanowire core. For high-aspect-ratio, densely spaced NW arrays, the resulting active region area per unit substrate area can be much larger than the unity active region areas per unit substrate area associated with planar structures. For LEDs, this enhanced active region area per unit substrate area can potentially enable lower active-region drive current densities for mitigating efficiency droop while still maintaining the high drive currents per unit substrate area desired for low cost per lumen. As a side benefit, for solar cells, this enhanced active region area per unit substrate area can potentially enable enhanced optical absorption per unit substrate area.

To explore the potential of such nanostructures, we fabricated and tested them both in LED and solar cell modes. The fabrication began with a dense array of nanowires top-down etched into an n-GaN substrate, then a regrowth of InGaN/GaN multiple quantum-well/quantum-barrier shells, followed by growth of a p-type InGaN canopy layer that connects the nanowires into a continuous film, and then finally metal contacts both to the p-type canopy as well as to the n-type substrate.

The final structure[33] (sans metal contacts) is shown in Figure 4. In LED mode, electroluminescence (EL) spectra show two

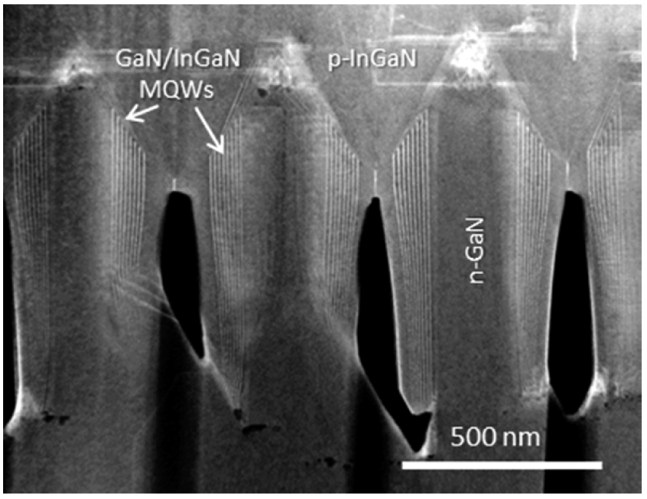

Figure 4. Cross-section STEM image of array of radial core−shell GaN/InGaN MQW nanowires for vertically integrated LEDs and solar cells.

distinct peaks: one centered at ~620 nm and one that shifts from ~605 to ~560 nm with increasing injection current.[34] In solar cell mode,[33] a photo response was observed out to 2.1 eV, the lowest energy of any III-nitride solar cell so far reported, with efficiencies of 0.3% that, while low, are the highest thus far reported for an InGaN NW solar cell.

To help elucidate the spatial variation in indium composition and to correlate this to the EL spectra, pulsed-laser atom probe tomography (APT) and cathodoluminescence (CL) measurements were made.[35] In contrast to the EL data, the CL data are dominated by relatively broad blue emission centered around 430−440 nm and originating from the nonpolar sidewalls. Weaker and longer wavelength emission is observed at the nonpolar nanowire tips by CL, suggesting that the yellow−red EL originates from the nanowire tip regions and not the nonpolar sidewall QWs due to preferential current flow. The interpretation of the APT measurements made use of our earlier studies showing that variations in polarity and differences in evaporation fields can lead to reconstruction artifacts.[36] The measurements revealed composition variations on several length scales: variation within the nonpolar side facet QWs (indium composition increasing from bottom to top) and variation between the nonpolar side and semipolar apex facets (higher indium content in the nonpolar side compared to the semipolar-apex facet QWs). It is these composition variations that give rise to the relatively broad spectra. As mentioned in a previous subsection, such composition variations can also be advantageous or disadvantageous depending on intended use.

Perhaps most importantly, APT analyses of indium and Mg-dopant clustering, and of interface morphology, reveal material microstructural quality comparable to that of planar LED QWs. This is consistent with the relative brightness of the CL, particularly from the nonpolar side facet QWs, though absolute efficiencies have yet to be quantified.

MATERIALS ARCHITECTURES: QUANTUM DOTS AND PHOSPHORS

Our "Quantum Dots and Phosphors" Research Challenge explores the synthesis and photoluminescence physics of efficient down-conversion materials, particularly those that absorb in the blue and emit in a narrow line width in the red. If such materials could be developed, the narrow-line-width phosphor technology challenge could be overcome. Two classes of down converters have been investigated: Eu^{3+}-doped tantalate phosphors and II–VI semiconductor quantum dots (QDs).

Eu^{3+}-Doped Tantalate Phosphors. As mentioned in the Introduction, the red phosphors currently utilized for SSL have a very broad emission, extending into the deep red where the human eye is not very sensitive—farther than is necessary for high color rendering. The requirements of such an improved red phosphor are several: broad absorption in the blue (~460 nm), narrow line width, high-quantum-yield emission in the red (~620 nm), and robustness to temperature.

In our work, we have developed a class of pyrochlore-type rare-earth tantalate nanoparticle phosphors of the form $KLnTa_2O_7$:RE, where Ln = (Y, Gd, Lu) and RE = a rare earth dopant. The small (nano) particle size of these phosphors reduces scattering losses, and the flexibility of the pyrochlore lattice enables tailoring optical properties, such as broadening the blue excitation line width. Most importantly, these phosphors can accommodate the Eu^{3+} rare-earth dopant in noncentrosymmetric sites, which can be directly excited by blue light and then emit narrow-band red emission.[37] Other Eu^{3+}-doped phosphors being explored for blue LED excitation include lanthanum niobates[38] and molybdates/tungstates.[39]

Not unsurprisingly, the detailed properties of the Eu^{3+}-doped tantalate phosphors do depend on the lanthanide. When Ln = Lu or Y, the pyrochlore structure was obtained, and quantum yields (QYs) of 63 and 67%, respectively, were obtained. When Ln = Gd, a distorted pyrochlore containing oxygen vacancies, with the composition $K_{12x}GdTa_2O_{7x}$:Eu ($x = 1/3$) and a QY of 78%, was obtained. The higher quantum yield is likely due to the larger ionic radius of Gd than that of Y or Lu, which leads to lattice distortion and a relaxation of the parity selection rule for the 4f–4f transitions in the red (~610–615 nm). Indeed, along with the higher quantum yield comes, for the same reasons, a desirable broader blue absorption line width (~9 nm).

To explore the influence of RE ionic radius r_{RE} on the luminescence and structure of tantalates further, we replaced Gd with La ($r_{La} > r_{Gd}$). The resulting $LaTaO_4$:Eu^{3+} phosphors are structurally unrelated to the pyrochlores and have even higher QYs (up to 88%).[40] These QYs are maintained up to Eu^{3+} concentrations of 25%, at which point additional tantalate phases with lower QYs form.[41] Moreover, these Eu^{3+}-doped rare-earth tantalates have low thermal quenching (only 3% at 130 °C) and excellent thermal and chemical stability due to their refractory nature.

For both the pyrochlores and La tantalates, though, their main limitation for SSL is low blue absorbance. In powder form, where scattering competes with absorption, this is a real limitation. However, it might be possible to fabricate the phosphors as transparent (nonscattering) wafers to increase the optical path length of blue light to the ~1 mm thicknesses needed for optimal absorption.

II–VI Quantum Dot Synthesis and Properties. As an alternative to phosphors, we have also been exploring semiconductor quantum dots (QDs). QDs have many attractive properties as wavelength down converters, including tunable narrow band emission, broad absorption, and high QYs.

In our work, we have explored core–multishell semiconductor QDs designed to emit in the red. For the cores, we nucleate then grow CdTe using standard high-temperature solution synthesis. For the multishells, selective ion layer absorption and reaction (SILAR)[42,43] is then used to coat these cores with successive shells of CdSe, CdS, and finally ZnS because ZnS is stable to oxidation. The initial shell of CdSe is only two monolayers, but this is sufficient to increase QY from ~50% to as high as 95% while simultaneously red-shifting the emission from 594 to 618 nm. Starting with yellow-emitting cores, the final CdTe/2CdSe/CdS/5ZnS core/shell/shell/shell QDs have peak emission at 613 nm with a reasonably narrow FWHM of 42 nm.

Two key and fundamental problems associated with these QDs (and similar QDs being explored in industry) are thermal and photoquenching: the tendency of QYs to decrease, sometimes permanently, when exposed to high temperatures and photon fluxes. The fundamental mechanisms of both of these phenomena are not understood; in our work we have been seeking to understand the first of these phenomena, thermal quenching. In particular, we have been seeking to understand reversible thermal quenching, as we have found that the addition of the final ZnS shell eliminates the irreversible part of the thermal quenching.[44]

To understand reversible thermal quenching, CdSe/ZnSe and CdTe/CdSe QDs were synthesized and functionalized with octadecylamine (ODA) or tributylphosphine (TBP). The temperature dependence of the QYs and time-resolved luminescence decays, along with room-temperature transient absorption spectroscopy, were then used to elucidate the thermal quenching mechanisms.

Two types of thermal quenching were identified. The first type is dynamic quenching, characterized by a reduction in the lifetime of the emission, and has been attributed to thermally activated carrier trapping and/or trap creation.[45] This mechanism operates when a parallel decay channel becomes increasingly significant at elevated temperatures. The second type is static quenching, characterized by a decrease in the initial amplitude of the decay curve, indicating an increase in the fraction of "dark" particles with increasing temperature. Both types can apply, but in our work thus far we have focused attention on the static quenching, which is predominant in our QDs.

We found that the mechanism for the static quenching is thermal promotion of valence band electrons to empty chalcogenide p orbitals on the particle surfaces (Figure 5a). This thermal promotion leaves a hole in the valence band, so that subsequent photoexcitation produces a positive trion. The trion undergoes relatively rapid nonradiative Auger recombination, rendering the particle dark (Figure 5b).[46] Ligands that bind to empty p orbitals on the particle surfaces minimize static thermal quenching up to temperatures of ~80 °C, but at higher

dx.doi.org/10.1021/jp501136j | J. Phys. Chem. C 2014, 118, 13330–13345

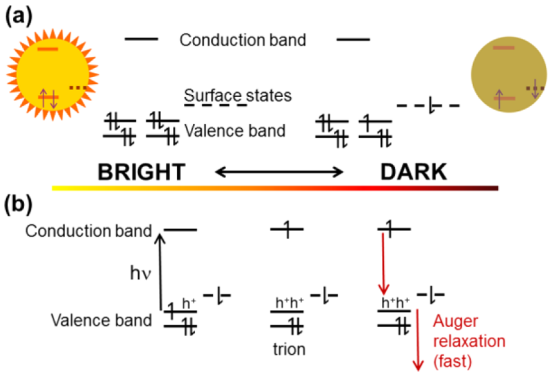

Figure 5. Mechanism for QD static thermal quenching. (a) Thermal equilibrium resulting in a surface charge state, leaving behind a hole in the valence band. (b) Subsequent photoexcitation produces an additional electron–hole pair, which relaxes via a nonradiative Auger process.

temperatures an excess of ligands in solution is required to prevent irreversible ligand loss.

This insight has enabled the design of quantum dot heterostructures with little to no thermal quenching. We now have developed CdTe/CdSe/ZnSe QDs with graded shells and that are surface rich in Zn. These QDs emit at 620 nm (nearly optimal for lighting), have a room temperature QY of about 75%, and show only 14% thermal quenching at 80 °C.

LIGHT-EMISSION PHENOMENA: COMPETING RADIATIVE AND NONRADIATIVE RECOMBINATION PROCESSES

Our "Competing Radiative and Nonradiative Recombination Processes" Research Challenge aims to develop a microscopic understanding of the competing physical processes that determine light-emission efficiency of InGaN materials and heterostructures. The radiative efficiency of a material is defined by the competition between radiative pathways and highly undesirable nonradiative pathways that produce heat instead of light. For InGaN materials, we find an array of potential nonradiative processes that may limit the radiative efficiency but are not well understood. With such understanding, new routes to ultrahigh light-emission efficiency at all current densities and all across the visible spectrum might be realized, thus overcoming the efficiency droop and RYG-gap technology challenges to high-efficiency solid-state lighting.

Our study of these competing physical processes involves both theory and experiment, with a particular focus on understanding the mechanisms behind the efficiency droop phenomenon. Notably, a range of nonradiative mechanisms have been proposed to explain efficiency droop in InGaN LEDs. Recent models[47,48] and experiments[49−51] lend increasing support for Auger recombination as the dominant nonradiative loss in the high-current regime. However, alternative mechanisms, including inefficient carrier injection into the active region,[52,53] carrier delocalization and recombination at defects,[54,55] and nonlinear recombination at multilevel defects,[56] have also been proposed. In our EFRC studies described below, we examine some of these alternative mechanisms while also evaluating and advancing carrier recombination models to better elucidate the factors limiting the efficiency of InGaN LEDs.

Models of Radiative Recombination Processes. As presented in Figure 2, the internal quantum efficiency (IQE) of an LED can be described by the expression: IQE = $Bn^2/(An + Bn^2 + Cn^3 + Dn^m + ...)$. Although strictly speaking an empirical expression, the individual terms correspond to different (physical) carrier recombination mechanisms that have corresponding functional dependences on carrier density n: An is ascribed to Shockley–Read–Hall nonradiative recombination, Bn^2 to bimolecular radiative recombination, Cn^3 to Auger nonradiative recombination, and Dn^m to other higher-order processes. To date, this "ABC model" has been the primary method to interpret experimental InGaN LED efficiency-versus-current data to gain insight into competing recombination mechanisms.[6] Our work in this Research Challenge has yielded new insights into the implications and limitations of the ABC model, as well as an advanced microscopic model that overcomes many of the ABC model deficiencies.

As one implication, we showed that the commonly applied ABC model predicts IQE versus carrier density curves with even symmetry, while experimental curves are typically asymmetric.[57] This departure from symmetry indicates that a nonradiative recombination term to the fourth power in carrier density ($\sim Dn^4$) or higher must be added to match experiment, shedding light on characteristics of nonradiative mechanisms not considered in the simple ABC model.

Using the ABC model for describing the recombination of carriers in InGaN QWs, we showed that the theoretical width of the radiative efficiency versus carrier concentration curve is related to the peak radiative efficiency.[58] Since the normalized external quantum efficiency EQE_{norm} is proportional to the radiative efficiency, and the square root of the light-output power is proportional to the carrier density n, the experimentally determined width of the EQE_{norm} vs n curve can be used to determine the radiative efficiency. These observations are significant in that they define a simplified experimental approach to determine the radiative efficiency of QWs. In contrast to typical approaches where the efficiency at room temperature is calibrated by the efficiency at 4 K (where peak efficiency is assumed to be 100%), the new approach relies solely on room-temperature measurements. We found that experimental excitation-dependent photoluminescence measurements on a blue-emitting InGaN QW sample yielded 91% peak efficiency, comparable to the value obtained using more labor-intensive temperature-dependent photoluminescence measurements (Figure 6).

A limitation of the ABC model is that it assumes constant recombination coefficients for radiative and nonradiative processes, an assumption that may not hold for InGaN materials at high carrier densities. In collaboration with our "Defect–Carrier Interactions" Research Challenge, we explored the potential for multilevel defects to yield carrier-density-dependent nonradiative recombination rates, thereby contributing to efficiency loss at high currents.[56] Details of these studies are included in the following section.

While insight can be attained via application of the ABC model, LED operation at high current densities involves a complex combination of carrier–carrier and carrier–phonon interactions and carrier-concentration-dependent recombination processes that cannot be fully captured by this simple model. To overcome some of the ABC model deficiencies, we developed a new microscopic model for investigating recombination processes in InGaN QWs and LEDs.[59] Key advances beyond the ABC model include direct inclusion of bandstructure, a microscopic description of spontaneous

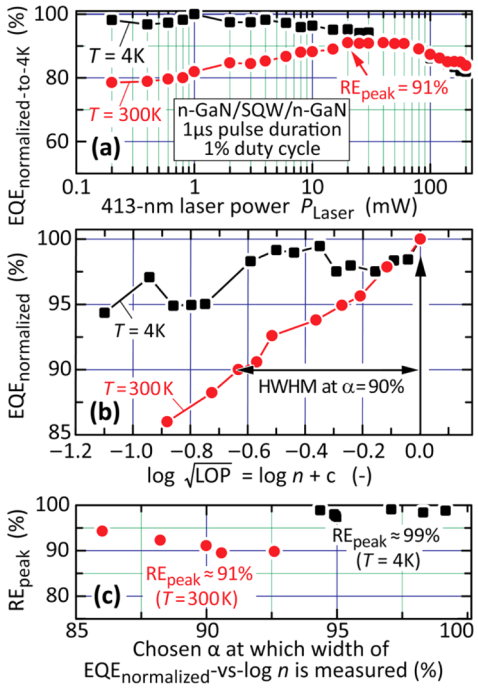

Figure 6. (a) Relative efficiency (RE) versus excitation-laser power at 4 K and 300 K for an n-type-GaN/SQW/n-type-GaN sample; the efficiency is normalized to the peak efficiency at 4 K. By assuming 100% efficiency at 4 K, one obtains a RE_{peak} of 91% at 300 K. (b) Normalized external quantum efficiency (EQE) obtained from the data shown in (a). The half-width can be used to determine RE_{peak}. (c) RE_{peak} determined from the half-width shown in (b). At T = 4 K, the sample shows a RE_{peak} of 99%, while at T = 300 K it shows a RE_{peak} of 91%, in agreement with the temperature-dependent PL results. (With permission from AIP Publishing, LLC.)

emission, and consistent treatment of carrier capture and escape at the level of carrier−carrier and carrier−phonon collisions.

We applied this model to the study of performance differences between violet and green InGaN LEDs, with a goal of gaining insight into contributions to the RYG gap. The simulations identified performance differences that arise at different current densities and temperatures due to variations in spontaneous emission rates and heat loss rates in the two LED structures. By tracking momentum-resolved carrier populations, rather than only total carrier density, these rate changes can, in turn, be traced to intrinsic contributions from bandstructure and plasma heating that lead to reduced efficiency for longer-wavelength LEDs.

We further applied our microscopic model to study the temperature dependence of IQE versus current density trends for InGaN LEDs.[60] The experimentally reported change in the shape of the IQE vs current density curve with changing temperature was relatively well described by our model. However, the distinct high-current-density trends for blue vs green LEDs could not be reproduced using a single set of fitting parameters, and efforts are ongoing to resolve this discrepancy.

Finally, as another modeling effort, we explored the potential of using genetic algorithms (GAs), in concert with a device simulator, to optimize InGaN LED heterostructures for high efficiency.[61] In this GA modeling, the fitness function governing design selection is the IQE multiplied by a weight function to favor designs that have high IQE at high current densities. We applied this modeling approach to identify QW active region and electron blocking layer (EBL) designs that yield improved efficiency droop behavior. Our model successfully predicted reduced efficiency droop with doping of fewer barriers, in agreement with our experimental results, described below. In addition, our model identified AlInGaN EBL designs with complex compositional grading to mitigate polarization field effects as another approach to reduce efficiency droop.[61]

Carrier Transport Contributions to Efficiency Droop. In addition to IQE, carrier injection efficiency into the InGaN quantum well active layers of an LED is a factor that can limit the overall power conversion efficiency (Figure 2). However, the complexities of how carrier transport impacts efficiency of InGaN LEDs, particularly at high currents relevant to efficiency droop, are not well understood. A major focus of our studies has therefore been to gain insight into carrier transport effects and to further determine if such effects could play a dominant role in the efficiency droop phenomenon. As a first study, we employed bandstructure and carrier transport modeling to understand how internal polarization fields impact carrier capture and efficiency droop of InGaN LEDs.[62] We combined these models with experimental efficiency-versus-current data of blue-emitting LEDs in which we employed tailored Si doping of GaN barriers to modify the effects of polarization fields on carrier transport through the multiple quantum well (MQW) active region.

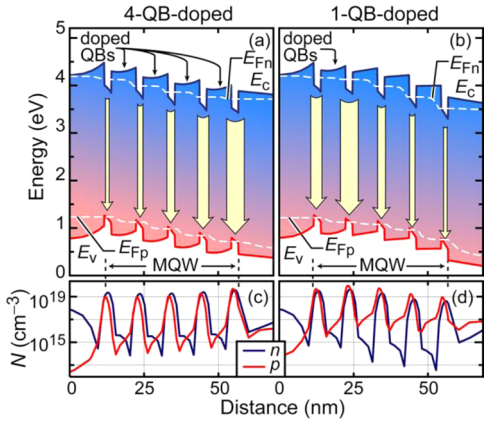

Figure 7. Simulated band profiles and illustration of the distribution of radiative recombination (arrows) within the MQW of InGaN/GaN LEDs with (a) 4-QB-doped (ND = 3 × 10^{18} cm^{-3}) and (b) 1-QB-doped structures at a forward current of 1 A (current density ∼1.1 kA cm^{-2}). Corresponding electron and hole concentration in the MQW active region for the (c) 4-QB-doped and (d) 1-QB-doped structures. (With permission from AIP Publishing, LLC.)

The LEDs in this study each had five InGaN QWs but differing number of Si-doped GaN barriers. Modeling using APSYS software[43] predicted that typical LED designs employing Si-doping in all GaN barriers have dominant carrier capture in the last (p-side) QW (Figure 7a, 7c; the right-most QW is closest to the p-type region) effectively increasing carrier density and non-radiative losses, e.g., Auger recombination. Doping only the first (*n*-side) barrier modifies the barrier potential profiles, shifting the recombination away from this problematic p-side QW (Figure 7b, 7d). Our experiments confirmed the benefit of this design, showing reduced efficiency droop in devices with fewer doped barriers, with ∼38% electroluminescence enhancement and reduced efficiency

dx.doi.org/10.1021/jp501136j | J. Phys. Chem. C 2014, 118, 13330−13345

droop in the design with one doped barrier vs four doped barriers.

In addition to strong polarization fields, III−N alloys are known to have a relatively strong asymmetry in electron and hole concentrations and mobilities. For InGaN LEDs under high injection conditions, this asymmetry leads to strong electron drift into the p-type layer, reducing overall quantum efficiency. Experimental efficiency versus current curves can then be well described by the inclusion of a drift-induced leakage term in the ABC recombination model. We showed that this term has a third- and fourth-order power dependence on carrier concentration in the active region, where the third-order term, C_{DL}, is estimated to be about 10^{-29} cm^6/s.[64]

While the efficiency droop phenomenon is largely associated with InGaN LEDs, we extended our studies to alternative III−V alloys where carrier transport asymmetry may also play a role.[65] Our studies confirmed that efficiency droop is not seen in AlInGaP red LEDs at room temperature. Quite notably, however, we found that efficiency droop is present in these LEDs at lower temperatures, a trend not predicted for Auger recombination. This observation was shown to be consistent with a drift-leakage contribution to efficiency droop, mediated by asymmetric carrier transport properties. In the case of AlInGaP, lower temperatures, where this asymmetry is enhanced due to stronger freeze-out of holes compared to electrons, are required to observe the droop behavior.

LIGHT-EMISSION PHENOMENA: DEFECT−CARRIER INTERACTIONS

Among the nonradiative recombination processes just discussed, defect-mediated recombination (associated with the A coefficient) is one believed to be particularly important, as it is present at all InGaN compositions and hence is a key issue for the RYG gap. Our "Defect−Carrier Interactions" Research Challenge thus aims to understand the electrical, optical, and structural properties of defects in InGaN materials and heterostructures. With such understanding, routes to circumventing defect contributions to nonradiative carrier recombination might be realized, helping to overcome the blue-efficiency and RYG-gap technology challenges.

Our studies have made use of two capabilities, both continuing to be developed.

The first capability is density functional theory, in which we are attempting to treat atomic configuration changes during carrier capture events, and not just with simplified one-dimensional coordinate models but with realistic multidimensional configurations.

The second capability is deep level optical spectroscopy (DLOS).[66] DLOS is a photocapacitance technique that uses sub-bandgap, monochromatic light to stimulate photoemission from deep-level defects located in the depletion region of the LED. The time derivative of the photocapacitance response at the instant illumination begins is proportional to the deep level optical cross-section (σ^o), which is the fundamental optical identifier of a defect state and can be thought of as the optical absorbance per unit defect. The optical deep-level energy in the bandgap (E^o) is determined by fitting the dependence of σ^o on photoexcitation energy to a theoretical model.[67] The defect density (N_t) within an individual QW is determined using the Poisson equation and the change in applied voltage (ΔV) required to maintain a fixed depletion depth at the QW upon defect photoemission.

Defects in InGaN QWs. In an initial study, we used DLOS to investigate the potential contribution of defects to the RYG efficiency gap.[68] Defects are a likely contributor to this gap because achieving longer-wavelength light emission requires increased indium incorporation, which in turn often requires lowered QW growth temperature (T_g). The lowered T_g can increase impurity (extrinsic defect) incorporation, and the increased strain associated with the higher indium content can drive excess intrinsic defect formation.

DLOS of blue- (~450 nm) and green-emitting (~530 nm) LEDs identified two deep level defects, one near-midbandgap and one near the valence band maximum. Both are believed to be associated with the InGaN QW deep levels because their density is much higher in the green-emitting than in the blue-emitting LED,[68] as illustrated in Figure 8a. The near-midbandgap QW deep level can be expected to reduce IQE by acting as a site for facile nonradiative recombination, while the defect state near the valence band maximum (E_v) can be expected to reduce EQE by acting as a hole trap that reduces injection efficiency. For the near-E_v QW defect states, carbon and Mg impurities are candidates because they are known to form near-E_v levels in GaN.[69,70] For the near-midgap InGaN QW defect, carbon and group-III vacancies are possible candidates because they have been established as deep-level centers in GaN.[71]

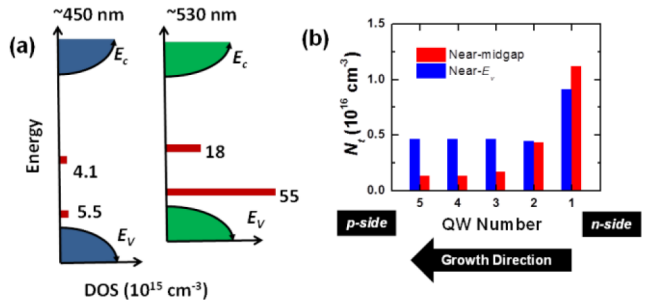

Figure 8. (a) Comparison between the average densities of states in the bandgap of InGaN QWs for blue- and green-emitting LEDs. Significantly enhanced defect density was observed in the green-emitting (higher indium content) LEDs. (b) Distribution of InGaN defect density among the multi QWs in the blue-emitting LED, showing higher defect densities in the first one or two QWs that were grown.

Defect Profiling in InGaN MQWs. In subsequent work, we adapted DLOS to measure the distribution of deep levels in MQW blue-light-emitting InGaN/GaN LEDs with nanoscale depth resolution.[72] The depth distribution of N_t in the MQW region was measured from the excess applied voltage (ΔV) required to maintain a constant capacitance and therefore a constant depletion depth (x_d) upon emptying a deep level upon illumination. $N_t(x_d)$ was then calculated from $\Delta V(x_d)$ data using the Poisson equation.

Figure 8b shows N_t of the near-midgap and near-E_v deep levels for each of five QWs in such an LED. The QWs were 2.5 nm thick and were spaced at a 10 nm period, demonstrating that DLOS is useful as a nondestructive defect spectroscopy with nanoscale resolution comparable to transmission electron microscopy. The cause of the defect "pile up" observed in the first few QWs is under further investigation, but hetero-interfaces[73] or indium incorporation itself[74] have been

dx.doi.org/10.1021/jp501136j | J. Phys. Chem. C 2014, 118, 13330−13345

suggested to sequester (or getter) defects to the benefit of subsequently grown QWs.

Multilevel Defects. As mentioned in the previous section on Competing Radiative and Nonradiative Recombination Processes, nonradiative recombination by defects is described by Shockley–Read–Hall (SRH) theory.[75,76]

A common limiting (and vastly simplified) case of SRH is the case of defects with only a single electronic level. In this case, the defect-mediated nonradiative recombination rate is linear in carrier density (n), and because other radiative and nonradiative recombination rates scale as n to higher powers, the relative impact of defects on LED efficiency becomes increasingly small with increasingly high drive currents and carrier densities.

However, in other cases, defects can have multiple electronic levels.[77] Defect-mediated nonradiative recombination in such cases can be superlinear in current and carrier densities and can thus be a contributor to droop-like behavior in LEDs.[56] In other words, it is possible for defects to influence LED performance even at high drive currents, despite the common assumption otherwise.

Defect Cross Sections for Carrier Capture. Computational studies of defects have typically focused on defect levels, which determine the relative rates of carrier capture and emission at a defect. However, at high carrier concentrations, carrier capture tends to overwhelm carrier emission, and the position of the defect level within the bandgap becomes less important than the carrier capture cross sections. We have developed procedures to calculate the activation energies that control carrier capture[78,79] both for simplified one-dimensional coordinate models and for realistic multidimensional configurations. Initial application of these models to the gallium vacancy gave results that agree well with experiments. Furthermore, the highest carrier densities and thus the majority of defect-induced recombination occur in the LED quantum wells.

LIGHT-EMISSION PHENOMENA: ENHANCED SPONTANEOUS EMISSION

In traditional 2D planar quantum-well architectures, spontaneous emission rates are largely determined by the materials themselves. In nanostructured architectures, however, spontaneous rates can be enhanced. Our "Enhanced Spontaneous Emission" Research Challenge explores ways in which spontaneous emission can be enhanced through modification of the environment within which the emission takes place (the Purcell effect[80]) and therefore ways in which spontaneous emission can better compete with parasitic nonradiative carrier recombination. If significant enough enhancements can be realized, routes might be developed to overcome the blue-efficiency and RYG-gap technology challenges. In addition, we are investigating routes to enhance quantum dot emission by coupling to metallic nanoparticles that could also impact the narrow-line-width red phosphor technology challenge.

Our current explorations focus on two nanophotonic approaches for modifying the emission environment: control of photonic density of states[81,82] (photonic crystals) and introduction of intense localized electromagnetic fields[83−86] (through plasmonics). Both approaches require integration of emitters with dielectric, plasmonic, or photonic crystal cavities, which we accomplish through nanofabrication and epitaxial growth (photonic crystals, fabricated metallic structures), chemical synthetic routes (core–shell dielectric/metallic spheres), or a combination of nanofabricated dielectric structures and assemblies of emitters (2D photonic crystals and QDs).

Fully 3D Semiconductor Photonic Crystals. Most previous work on visible photonic crystals (PCs) has focused: (a) on materials like titanium dioxide that are transparent in the visible but with relatively low ($n \sim 2.5$) refractive indices that restrict the magnitude of photonic crystal effects and (b) on 2D geometries that are easier to fabricate but do not offer full 3D light control.

To overcome these limitations, we have explored a fully 3D photonic crystal fabricated in Si semiconductor material.[87] Si has the two advantages of: (a) the maturity of the techniques with which it can be processing and (b) its high ($n \sim 3.5$) refractive index, which enables a large photonic strength (wide photonic bandgap, large photonic density of states).

Of course, because Si absorbs in the visible, it would not normally be considered applicable for SSL. However, we have experimentally demonstrated that the practical operational frequency range of a silicon-based 3D photonic crystal can be extended nearly into the visible (to about 700 nm), ∼400 nm above the absorption edge of silicon, due to the slow increase in the imaginary part of the refractive index (k) with decreasing wavelength. Moreover, we demonstrated that embedded defect structures in such Si logpile PCs can be used to create cavity modes within the photonic bandgap, thus paving the way to studying interactions between emitters in such cavities with artificially tailored photonic densities of states.

In subsequent work, we explored a fully 3D photonic crystal fabricated in GaN semiconductor material,[88] as illustrated in Figure 9. This tour-deforce nine-layer logpile 3D photonic crystal (3DPC) was composed of single-crystalline GaN nanorods ∼100 nm in size grown epitaxially using sequential lithography and selective-area MOCVD. Optical measurements along the stacking direction showed a wide photonic bandgap in the visible (between 380 and 500 nm). The realization of III–N-based 3DPCs (and ultimately cavities) opens the door to the possibility of full 3D control of the spontaneous emission rate of nitride emitters.[87,88]

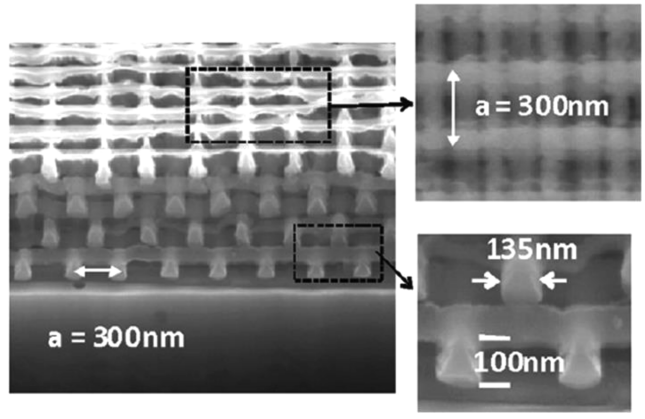

Figure 9. Cross-section SEM image of a nine-layer GaN logpile with a 300 nm lattice constant and rod height of 100 nm at lower pressure optimal growth conditions to enable nucleation on the GaN epilayer resulting in a 2D growth mode. The top right-hand side image shows an enlarged top view, and the bottom image shows an enlarged section of the perspective view of regions indicated by a dotted black box. The width of the rod is approximately 135 nm.

Plasmonic Dipole Nanoantennas. The use of plasmonic antennas in light-emitting semiconductor devices has been

extensively explored in recent years. Such antennas enhance both radiative recombination within the device as well as the out-coupling of that radiation into free space. In this research, we are exploring the potential of plasmonic antennas for enhancing spontaneous emission from emitters with lower-than-ideal internal quantum efficiency. We are using computational finite-difference time-domain (FDTD) simulations to study idealized nanophotonic emitters that are embedded in materials with various refractive indices; are coupled to half-dipole Ag antennas with optimized geometries; and emit light at the four (red, yellow, green, blue) wavelengths of greatest interest to SSL. The work is in progress, but preliminary results indicate that plasmonic antennas have some promise in the red (where Joule losses are lower) but less so in the yellow, green, and blue (where Joule losses are higher).

Core–Shell Plasmonic Antennas. An alternative use of plasmonics is not in electroluminescent structures, as studied above, but in photoluminescent structures useful for wavelength downconversion. We have done some exploratory work in core–shell plasmonic geometries, in which the emitter is the core and the metal is the shell (rather than the more usual opposite configuration). This geometry has many advantages, such as uniformity of the enhanced optical field inside, lack of polarization sensitivity, and environmental protection of the emitter. In addition, this core–shell structure is ideal for decoupling the enhancements of the absorption and emission processes.

For a 633 nm dye core surrounded by a Au shell, we find that the optimal ratio between the shell thickness and the inner radius is approximately 0.3 when the excitation wavelength is 632 nm. When this ratio is fixed at the optimal value, larger core radius and shell thickness produce greater intensity enhancement, with total fluorescence enhancements of ∼25 possible. The geometry discussed here is well-suited to red rare-earth phosphors used in SSL today, as it promises to greatly enhance their effective absorption cross section.[89]

LIGHT-EMISSION PHENOMENA: BEYOND SPONTANEOUS EMISSION

Because of nonradiative processes, such as Auger recombination, which become more pronounced at high carrier densities, it is of interest to explore radiative recombination processes that can outcompete these nonradiative processes. Enhanced spontaneous emission, as discussed in the previous section, is one possibility. Stimulated emission is yet another. Our "Beyond Spontaneous Emission" Research Challenge is focused on exactly this: exploring the possibility that lasers, based on stimulated emission, can provide a route to high efficiency. Indeed, beyond potentially high efficiency, lasers have other possible benefits, including ease of mixing and directing and focusing of the light. If these benefits could be realized across the visible spectrum, they could provide new routes to overcoming the blue-efficiency, RYG-gap, and enhanced functionality SSL technology challenges.

However, laser light sources for SSL are in their infancy, and much work needs to be done to understand both their potential and their limitations. In this Research Challenge several different aspects of light generation have been investigated where the common theme is that the light generation mechanism is not the standard spontaneous emission used in commercially available white light LEDs. First, we investigated the quality of the white light produced by mixing four different laser wavelengths to determine its suitability for general illumination. Second, we investigated the limits of efficiency improvements that are possible using lasers for solid-state lighting. Third, lasing from nanowire structures was investigated since nanowire lasers hold the promise for low-threshold, high-efficiency operation at wavelengths extending from the blue to the red.

Four-Color Laser Illuminant. One of the first issues we addressed in this Research Challenge was the quality of white light produced by mixing four laser beams composed of red, yellow, green, and blue wavelengths. One might anticipate that white light composed of very narrow line width (∼1 nm) lasers would not render colors as well as white light with a broader spectrum. Thus, even if lasers all across the visible spectrum were much more efficient and economical than LEDs, they might not be useful for solid-state lighting.

To experimentally investigate this question, we constructed a four-color laser illuminant,[8] composed of commercial lab-grade lasers with wavelengths of 635, 589, 532, and 457 nm. Color mixing optics were then used to create a laser-based white light source as illustrated in Figure 10. Side-by-side viewing booths

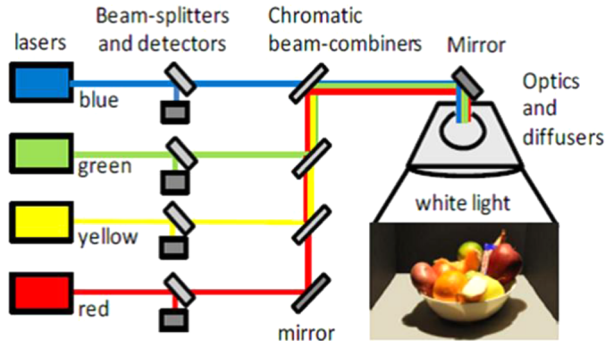

Figure 10. Schematic of a four-color laser-based white illuminant. Light from four lasers is combined using chromatic bean splitters, then passes through multiple ground glass diffusers to eliminate laser speckle before illuminating test objects. (With permission of The Optical Society.)

were set up such that observers could compare scenes illuminated either with commercial white light LEDs, incandescent lamps, or the laser illuminant.

The results were that the four-color laser white illuminant was virtually indistinguishable from state-of-the-art white reference illuminants. This result can be understood in terms of the broadband nature of the reflectance spectra from most everyday objects, as well as the broad wavelength response of the cones in the human eye. This study thus showed that white light produced using lasers was of high enough quality to be considered for solid-state lighting.

Blue Laser Diode versus Blue LED Trade-Offs. As just discussed, the ultimate illuminant might be very efficient color-mixed RYGB lasers. However, even without lasers in the red, yellow, and green, a blue laser diode (LD) might also have advantages over a blue LED as the pump source in the current wavelength-downconversion paradigm for SSL. To understand these advantages, as well as limitations, we performed a detailed and self-consistent analysis of the current states of the art for blue LEDs and LDs, along with the potential of both for future improvement.

This investigation, together with a detailed economic analysis, indicates that blue lasers have some compelling advantages over blue LEDs for SSL.[90] Compared to

dx.doi.org/10.1021/jp501136j | J. Phys. Chem. C 2014, 118, 13330–13345

spontaneous emission, stimulated emission is an ultrafast recombination process—so fast that it clamps carrier densities above the lasing threshold, clamps the rates of nonradiative recombination processes (such as Auger) that depend on carrier density, and, well above the threshold, easily outcompetes these nonradiative recombination processes. Thus, lasers can circumvent efficiency droop associated with parasitic nonradiative recombination. This enables LDs to operate in the regime of much higher input power densities than LEDs, in which much higher areal chip costs can be tolerated.

However, LDs do have other sources of efficiency loss. Among these are parasitic resistance loss associated with very high current densities and loss associated with small residual optical absorption within the laser cavity. There thus appear to be opportunities for novel (perhaps nanophotonic) laser designs that decrease current densities and optical losses via carrier, mode, and gain engineering.

Nanowire Lasers. Nanowires (NWs) also show promise as a future platform for efficient lasers and light generation.[91−93] As described in the "Nanowires" Research Challenge, NWs can be dislocation free and can have enhanced In incorporation, making them suitable for emission at wavelengths from the blue to the red. Semiconductor nanowires have recently seen application as plasmonic nanolasers.[94,95] In addition, NWs are attractive candidates for efficiency and compactness, being able to simultaneously function as a standalone optical cavity and gain medium. Furthermore, with the appropriate geometry and lattice spacing, an array of nanowires can behave as a photonic crystal.[96,97] For particular designs, lasers can be realized.

In our work, we have explored lasing of single NWs as well as arrays of NWs, thus far all via optical pumping.

For our single-NW lasers, the GaN NW forms the optical cavity with facets on each end of the wire, as well as providing the gain medium. Although not obviously of central importance for SSL, single-mode behavior is of interest for many other applications, and so we have explored some of the conditions for such single-mode behavior. We find that, for smaller NWs, single-mode operation is preserved far above the lasing threshold.[18] For larger nanowires, multimode operation occurs, so alternate methods for achieving single-mode lasing are needed.

One method for achieving single-mode operation is to place (using nanoprobe manipulation) two NWs of different lengths, which individually exhibit multimode behavior, side-by-side in close proximity to form a coupled cavity.[98] The coupling between the nanowire pair provides a mode selection mechanism through the Vernier effect and generates stable single-mode operation. Another method for achieving single-mode operation was to simply place the NW onto a gold film.[99] Due to the mode-dependent losses induced by the gold substrate, only a single transverse mode has a loss low enough to be overcome by the laser gain, thus enabling single-mode behavior. The observed increase in lasing threshold of only ∼13% after placement onto gold indicates that the impact of metal contacts on the optoelectronic properties is modest.

For arrays of NWs, we have explored the use of 2D NW photonic crystals (2DPCs) to provide lateral feedback for lasing. Because the wavelength at which lateral feedback occurs is determined by the photonic crystal geometry, lasers of different wavelengths can be fabricated on a single chip. Moreover, due to the relatively broad gain bandwidth of III−nitride quantum wells and the lateral nature of the feedback, the wavelength tuning range of the lasers can be quite large: a remarkable 60 nm of wavelength tuning was demonstrated on a single chip from a single epitaxial growth.[100]

SUMMARY

Solid-state lighting is an emerging technology that has made enormous progress this past decade and that has much room for further progress. The Energy Frontier Research Center for Solid-State Lighting Science aims (a) to help advance the scientific understanding of materials architectures and light-emission phenomena used in the current state-of-the-art solid-state lighting and (b) to explore new materials architectures and light-emission phenomena with the potential for dramatic improvements in electricity-to-light conversion efficiency. To do this, the SSLS EFRC is organized around six Research Challenges, two focused on materials architectures and four focused on light-emission phenomena.

In the EFRC's two materials architecture Research Challenges, among the most significant advances have been the following.

First, methods have been developed for combined bottom-up, top-down nanofabrication of large-area, uniform arrays of straight and smooth III−N nanowires into which axial heterostructures can be embedded and onto which coaxial structures can also be grown. These methods, particularly when aided by atomic-scale nanocharacterization and computational simulation of synthesis and optoelectronic properties, have much potential to enable 3D tailored nano- and mesomaterials architectures that can fill the RYG gap.

Second, a new class of Eu^{3+} phosphor with absorption in the blue and narrow emission in the red has been developed, and the dominant mechanism for the well-known but previously poorly understood thermal quenching in II−VI quantum dots has been elucidated. Both of these advances may help enable new generations of wavelength downconversion materials that can solve the deep-red spillover wavelength-downconversion challenge.

In the EFRC's four light-emission phenomena Research Challenges, among the most significant advances have been the following.

First, "beyond ABC" microscopic models of carrier recombination have been developed that include many-body carrier interactions, carrier transport, strain and polarization fields, Auger recombination, and defects in both quantum wells and quantum barriers. These models complicate but also provide a more nuanced view of the physical processes that can compete with each other for carrier recombination.

Second, deep-level optical spectroscopy techniques were developed that can quantify defect densities in individual InGaN quantum wells, and models were developed that indicate that point defects with multiple charge levels can lead to recombination rates that are highly nonlinear with carrier concentration and that can be a contributor to efficiency droop.

Third, a fully 3D photonic crystal was fabricated in GaN semiconductor material, opening the door to the possibility of full 3D enhancement and control of the spontaneous emission rate of nitride emitters, perhaps enabling spontaneous emission to outcompete parasitic nonradiative recombination processes.

Fourth, through detailed simulations and human factors studies, lasers have been identified as a promising alternative to LEDs for solid-state lighting, both as a blue or UV pump for wavelength downconversion, as well as for RYGB color mixing. This paves the way for more serious efforts to understand the

dx.doi.org/10.1021/jp501136j | J. Phys. Chem. C 2014, 118, 13330−13345

limits to efficiency of both LEDs *and* lasers as well as architectures at the boundary between LEDs and lasers.

AUTHOR INFORMATION

Corresponding Author

*Phone: 505-844-7843. E-mail: mecoltr@sandia.gov.

Author Contributions

The manuscript was written through contributions of all authors.

Notes

The authors declare no competing financial interest.

Biographies

Michael E. Coltrin is Director of the Energy Frontier Research Center for Solid-State Lighting Science and a Distinguished Member of Technical Staff (DMTS) at Sandia National Laboratories. His research focuses on kinetics and morphology evolution in the growth of semiconductor materials. He received his PhD in Physical Chemistry from the University of Illinois at Urbana.

Andrew M. Armstrong is a Principal Member of Technical Staff (PMTS) at Sandia National Laboratories. His research is centered on development and application of deep-level optical spectroscopy of III−nitride materials. He received his PhD in Electrical and Computer Engineering from Ohio State University.

Igal Brener is a DMTS at Sandia National Laboratories. His research deals with fundamental and applied aspects of metamaterials, plasmonics, and other nanophotonics phenomena. He received his PhD in Physics from Technion, Haifa, Israel.

Weng W. Chow is a DMTS at Sandia National Laboratories, where his primary research involves applying microscopic theory to semiconductor laser development. He received his PhD in Physics from the University of Arizona.

Mary H. Crawford is a Senior Scientist at Sandia National Laboratories. Her research interests are currently centered on nitride-based materials and optoelectronic devices. She received her PhD in Physics from Brown University.

Arthur J. Fischer is a PMTS at Sandia National Laboratories, conducting research on emission physics and optical characterization of nitride-semiconductor materials and devices. He received his PhD in Physics from Oklahoma State University.

David F. Kelley is Professor and Founding Faculty in the Chemistry and Chemical Biology Department at the University of California, Merced. His research group uses ultrafast optical spectroscopy to examine the optical and electronic properties of semiconducting nanoparticles. He received his PhD in Physical Chemistry from the University of Washington.

Daniel D. Koleske is a PMTS at Sandia National Laboratories. His research includes MOCVD growth of nitride semiconductors for SSL, with interest in growth kinetics and morphology evolution. He received his PhD in Physical Chemistry from the University of Chicago.

Lincoln J. Lauhon is Professor and Associate Chair of the Department of Materials Science and Engineering at Northwestern University. His research group pursues advances in the synthesis and characterization of new nanostructured materials. He received his PhD in Physics from Cornell University.

James E. Martin is a DMTS at Sandia National Laboratories. His research interests include investigations of the recombination dynamics and luminescence of quantum dots and nanophosphors. He received his PhD in Physical Chemistry from the University of Washington.

May Nyman is Associate Professor in the Department of Chemistry at Oregon State University. Her research interests include inorganic ion exchangers, niobates and tantalates, luminescent materials, and inorganic polyanions and polycations. She received her PhD in Chemistry from the University of New Mexico.

E. Fred Schubert is Wellfleet Senior Constellation Professor of the Future Chips Constellation with appointments in the Electrical Engineering and Physics Departments at Rensselaer Polytechnic Institute. His primary research interest is in the field of compound semiconductor materials and devices. He received his PhD in Electrical Engineering at the University of Stuttgart.

Lauren E. Shea-Rohwer is a PMTS at Sandia National Laboratories. Her research currently includes phosphor powders and films and nanoscale luminescent materials such as II−VI quantum dots. She received her PhD in Materials Science from the University of California at San Diego.

Ganapathi Subramania is a PMTS at Sandia National Laboratories. His research interest involves exploring light−matter interaction inside nanostructured environments like photonic crystals and metamaterials. He received his PhD in Electrical Engineering and Applied Physics from Iowa State University.

Jeffrey Y. Tsao is Chief Scientist of the Energy Frontier Research Center for Solid-State Lighting Science and a DMTS at Sandia National Laboratories. His research involves integrated science, technology, and economic modeling in solid-state lighting and other areas. He received his PhD in Applied Physics from Harvard University.

George T. Wang is a PMTS at Sandia National Laboratories. His primary research efforts focus on the synthesis, characterization, and applications of III−nitride nanowires grown by MOCVD. He received his PhD in Chemical Engineering from Stanford University.

Jonathan J. Wierer, Jr. is a PMTS at Sandia National Laboratories, where he conducts research on III−nitride material properties and developing novel optoelectronic devices. He received his PhD in Electrical Engineering from the University of Illinois at Urbana.

Jeremy B. Wright is a graduate student at the University of New Mexico's Center for High Technology Materials, the University of New Mexico, and Sandia National Laboratories. His work focuses on optoelectronic properties of novel III−nitride nanostructures.

ACKNOWLEDGMENTS

This work was supported by Sandia's Solid-State Lighting Science Energy Frontier Research Center, sponsored by the Department of Energy Office of Basic Energy Science. Sandia National Laboratories is a multiprogram laboratory managed and operated by Sandia Corporation, a wholly owned subsidiary of Lockheed Martin Company, for the United States Department of Energy's National Nuclear Security Administration under Contract DE-AC04-94AL85000.

REFERENCES

(1) Tsao, J. Y.; Waide, P. The World's Appetite for Light: Empirical Data and Trends Spanning Three Centuries and Six Continents. *Leukos* **2010**, *6*, 259−281.

(2) *Solid-State Lighting Research and Development Multi-Year Program Plan*; April, 2013, 2013.

(3) Crawford, M. H.; Wierer, J. J.; Fischer, A. J.; Wang, G. T.; Koleske, D. D.; Subramania, G.; Coltrin, M. E.; Tsao, J. Y.; Karlicek, R.

F. Solid-State Lighting: Toward Smart and Ultra-Efficient Materials, Devices, Lamps and Systems. In *Photonics: Photonics Technology and Instrumentation*, Andrews, D. L., Ed. Wiley: New York, 2014; Vol. 3.
(4) Tsao, J. Y.; Coltrin, M. E.; Crawford, M. H.; Simmons, J. A. Solid-State Lighting: An Integrated Human Factors, Technology, and Economic Perspective. *Proc. IEEE* **2010**, *98*, 1162−1179.
(5) Narukawa, Y.; Ichikawa, M.; Sanga, D.; Sano, M.; Mukai, T. White Light Emitting Diodes with Super-High Luminous Efficacy. *J. Phys. D: Appl. Phys.* **2010**, *43*, 354002.
(6) Piprek, J. Efficiency Droop in Nitride-Based Light-Emitting Diodes. *Phys. Status Solidi (a)* **2010**, *207*, 2217−2225.
(7) Phillips, J. M.; Coltrin, M. E.; Crawford, M. H.; Fischer, A. J.; Krames, M. R.; Mueller-Mach, R.; Mueller, G. O.; Ohno, Y.; Rohwer, L. E.; Simmons, J. A. Research Challenges to Ultra-Efficient Inorganic Solid-State Lighting. *Laser Photonics Rev.* **2007**, *1*, 307−333.
(8) Neumann, A.; Wierer, J. J., Jr.; Davis, W.; Ohno, Y.; Brueck, S. R. J.; Tsao, J. Y. Four-Color Laser White Illuminant Demonstrating High Color-Rendering Quality. *Opt. Express* **2011**, *19*, A982−A990.
(9) Schubert, E. F.; Kim, J. K. Solid-State Light Sources Getting Smart. *Science* **2005**, *308*, 1274−1278.
(10) Yan, R.; Gargas, D.; Yang, P. Nanowire Photonics. *Nat. Photonics* **2009**, *3*, 569−576.
(11) Li, S.; Waag, A. GaN Based Nanorods for Solid State Lighting. *J. Appl. Phys.* **2012**, *111*, 071101.
(12) Duan, X.; Lieber, C. M. Laser-Assisted Catalytic Growth of Single Crystal GaN Nanowires. *J. Am. Chem. Soc.* **2000**, *122*, 188−189.
(13) Kuykendall, T.; Pauzauskie, P.; Lee, S.; Zhang, Y.; Goldberger, J.; Yang, P. Metalorganic Chemical Vapor Deposition Route to GaN Nanowires with Triangular Cross Sections. *Nano Lett.* **2003**, *3*, 1063−1066.
(14) Hersee, S. D.; Sun, X.; Wang, X. The Controlled Growth of GaN Nanowires. *Nano Lett.* **2006**, *6*, 1808−1811.
(15) Li, Q.; Wang, G. T. Improvement in Aligned GaN Nanowire Growth Using Submonolayer Ni Catalyst Films. *Appl. Phys. Lett.* **2008**, *93*, 043119−043119−3.
(16) Wang, G. T.; Talin, A. A.; Werder, D. J.; Creighton, J. R.; Lai, E.; Anderson, R. J.; Arslan, I. Highly Aligned, Template-Free Growth and Characterization of Vertical GaN Nanowires on Sapphire by Metal−Organic Chemical Vapour Deposition. *Nanotechnology* **2006**, *17*, 5773.
(17) Wagner, R.; Ellis, W. Vapor-Liquid-Solid Mechanism of Single Crystal Growth. *Appl. Phys. Lett.* **1964**, *4*, 89−90.
(18) Li, Q.; Wright, J. B.; Chow, W. W.; Luk, T. S.; Brener, I.; Lester, L. F.; Wang, G. T. Single-Mode GaN Nanowire Lasers. *Opt. Express* **2012**, *20*, 17873−17879.
(19) Li, Q.; Westlake, K. R.; Crawford, M. H.; Lee, S. R.; Koleske, D. D.; Figiel, J. J.; Cross, K. C.; Fathololoumi, S.; Mi, Z.; Wang, G. T. Optical Performance of Top-Down Fabricated InGaN/GaN Nanorod Light Emitting Diode Arrays. *Opt. Express* **2011**, *19*, 25528−25534.
(20) Baird, L.; Ong, C. P.; Cole, R. A.; Haegel, N. M.; Talin, A. A.; Li, Q.; Wang, G. T. Transport Imaging for Contact-Free Measurements of Minority Carrier Diffusion in GaN, GaN/AlGaN, and GaN/InGaN Core-Shell Nanowires. *Appl. Phys. Lett.* **2011**, *98*, 132104.
(21) Huang, J. Y.; Zheng, H.; Mao, S. X.; Li, Q.; Wang, G. T. In Situ Nanomechanics of GaN Nanowires. *Nano Lett.* **2011**, *11*, 1618−1622.
(22) Greer, J. R.; Nix, W. D. Nanoscale Gold Pillars Strengthened Through Dislocation Starvation. *Phys. Rev. B* **2006**, *73*, 245410.
(23) Shan, Z.; Mishra, R. K.; Asif, S. S.; Warren, O. L.; Minor, A. M. Mechanical Annealing and Source-Limited Deformation in Submicrometre-Diameter Ni Crystals. *Nat. Mater.* **2007**, *7*, 115−119.
(24) Uchic, M. D.; Dimiduk, D. M.; Florando, J. N.; Nix, W. D. Sample Dimensions Influence Strength and Crystal Plasticity. *Science* **2004**, *305*, 986−989.
(25) Volkert, C. A.; Lilleodden, E. T. Size Effects in the Deformation of Sub-Micron Au Columns. *Philos. Mag.* **2006**, *86*, 5567−5579.
(26) Zhu, T.; Li, J. Ultra-Strength Materials. *Prog. Mater. Sci.* **2010**, *55*, 710−757.
(27) Greer, J. R.; De Hosson, J. T. M. Plasticity in Small-Sized Metallic Systems: Intrinsic Versus Extrinsic Size Effect. *Prog. Mater. Sci.* **2011**, *56*, 654−724.
(28) Li, Q.; Wang, G. T. Strain Influenced Indium Composition Distribution in GaN/InGaN Core-Shell Nanowires. *Appl. Phys. Lett.* **2010**, *97*, 181107.
(29) Mukai, T.; Yamada, M.; Nakamura, S. In *InGaN-Based Uv/Blue/Green/Amber LEDs, Optoelectronics' 99-Integrated Optoelectronic Devices*; International Society for Optics and Photonics: Washington, 1999; pp 2−13.
(30) Pereira, S.; Correia, M.; Pereira, E.; O'Donnell, K.; Trager-Cowan, C.; Sweeney, F.; Alves, E. Compositional Pulling Effects in in(X)Ga(1-X)N/GaN Layers: A Combined Depth-Resolved Cathodoluminescence and Rutherford Backscattering/Channeling Study. *Phys. Rev. B* **2001**, *64*, 205311.
(31) Wong, B. M.; Leonard, F.; Li, Q.; Wang, G. T. Nanoscale Effects on Heterojunction Electron Gases in GaN/AlGaN Core/Shell Nanowires. *Nano Lett.* **2011**, *11*, 3074−3079.
(32) Wang, C.-Y.; Chen, L.-Y.; Chen, C.-P.; Cheng, Y.-W.; Ke, M.-Y.; Hsieh, M.-Y.; Wu, H.-M.; Peng, L.-H.; Huang, J. GaN Nanorod Light Emitting Diode Arrays with a Nearly Constant Electroluminescent Peak Wavelength. *Opt. Express* **2008**, *16*, 10549−10556.
(33) Wierer, J. J., Jr.; Li, Q.; Koleske, D. D.; Lee, S. R.; Wang, G. T. III- Nitride Core-Shell Nanowire Arrayed Solar Cells. *Nanotechnology* **2012**, *23*, 194007.
(34) Wang, G. T.; Li, Q.; Wierer, J. J.; Koleske, D. D.; Figiel, J. J. Top−Down Fabrication and Characterization of Axial and Radial III-Nitride Nanowire LEDs. *Phys. Status Solidi (a)* **2014**, *211*, 748−751.
(35) Riley, J. R.; Padalkar, S.; Li, Q.; Lu, P.; Koleske, D. D.; Wierer, J. J.; Wang, G. T.; Lauhon, L. J. Three-Dimensional Mapping of Quantum Wells in a GaN/InGaN Core−Shell Nanowire Light-Emitting Diode Array. *Nano Lett.* **2013**, *13*, 4317−4325.
(36) Riley, J. R.; Bernal, R. A.; Li, Q.; Espinosa, H. D.; Wang, G. T.; Lauhon, L. J. Atom Probe Tomography of a-Axis GaN Nanowires: Analysis of Nonstoichiometric Evaporation Behavior. *ACS Nano* **2012**, *6*, 3898−3906.
(37) Nyman, M.; Rodriguez, M. A.; Shea-Rohwer, L. E.; Martin, J. E.; Provencio, P. P. Highly Versatile Rare Earth Tantalate Pyrochlore Nanophosphors. *J. Am. Chem. Soc.* **2009**, *131*, 11652−11653.
(38) Francis, L. T.; Rao, P. P.; Thomas, M.; Mahesh, S.; Reshmi, V.; Thampi, V. D. New Orange-Red Emitting Phosphor La3NbO7: Eu3+ Under Blue Excitation. *Mater. Lett.* **2012**, *81*, 142−144.
(39) Dutta, P.; Khanna, A. Eu3+ Activated Molybdate and Tungstate Based Red Phosphors with Charge Transfer Band in Blue Region. *ECS J. Solid State Sci. Technol.* **2013**, *2*, R3153−R3167.
(40) Nyman, M.; Rodriguez, M. A.; Rohwer, L. E.; Martin, J. E.; Waller, M.; Osterloh, F. E. Unique LaTaO4 Polymorph for Multiple Energy Applications. *Chem. Mater.* **2009**, *21*, 4731−4737.
(41) Bleier, G. C.; Nyman, M.; Rohwer, L. E. S.; Rodriguez, M. A. Seeking the Optimal LaTaO4:Eu Phosphor. *J. Solid State Chem.* **2011**, *184*, 3221−3227.
(42) Li, J. J.; Wang, Y. A.; Guo, W.; Keay, J. C.; Mishima, T. D.; Johnson, M. B.; Peng, X. Large-Scale Synthesis of Nearly Monodisperse Cdse/Cds Core/Shell Nanocrystals Using Air-Stable Reagents Via Successive Ion Layer Adsorption and Reaction. *J. Am. Chem. Soc.* **2003**, *125*, 12567−12575.
(43) Xie, R.; Kolb, U.; Li, J.; Basché, T.; Mews, A. Synthesis and Characterization of Highly Luminescent Cdse-Core Cds/Zn0. 5cd0. 5s/Zns Multishell Nanocrystals. *J. Am. Chem. Soc.* **2005**, *127*, 7480−7488.
(44) Shea-Rohwer, L. E.; Martin, J. E.; Cai, X.; Kelley, D. F. Red-Emitting Quantum Dots for Solid-State Lighting. *ECS J. Solid State Sci. Technol.* **2013**, *2*, R3112−R3118.
(45) Zhao, Y.; Riemersma, C.; Pietra, F.; Koole, R.; de Mello Donegá, C.; Meijerink, A. High-Temperature Luminescence Quenching of Colloidal Quantum Dots. *ACS Nano* **2012**, *6*, 9058−9067.
(46) Cai, X.; Martin, J. E.; Shea-Rohwer, L. E.; Gong, K.; Kelley, D. F. Thermal Quenching Mechanisms in II-VI Semiconductor Nanocrystals. *J. Phys. Chem. C* **2013**, *117*, 7902−7913.
(47) Kioupakis, E.; Rinke, P.; Delaney, K. T.; Van de Walle, C. G. Indirect Auger Recombination as a Cause of Efficiency Droop in Nitride Light-Emitting Diodes. *Appl. Phys. Lett.* **2011**, *98*, 161107.

(48) Vaxenburg, R.; Rodina, A.; Lifshitz, E.; Efros, A. L. The Role of Polarization Fields in Auger-Induced Efficiency Droop in Nitride-Based Light-Emitting Diodes. *Appl. Phys. Lett.* **2013**, *103*, 221111.
(49) Shen, Y.; Mueller, G.; Watanabe, S.; Gardner, N.; Munkholm, A.; Krames, M. Auger Recombination in InGaN Measured by Photoluminescence. *Appl. Phys. Lett.* **2007**, *91*, 141101.
(50) Iveland, J.; Martinelli, L.; Peretti, J.; Speck, J. S.; Weisbuch, C. Direct Measurement of Auger Electrons Emitted from a Semiconductor Light-Emitting Diode Under Electrical Injection: Identification of the Dominant Mechanism for Efficiency Droop. *Phys. Rev. Lett.* **2013**, *110*, 177406.
(51) Binder, M.; Nirschl, A.; Zeisel, R.; Hager, T.; Lugauer, H.-J.; Sabathil, M.; Bougeard, D.; Wagner, J.; Galler, B. Identification of Nnp and Npp Auger Recombination as Significant Contributor to the Efficiency Droop in (Gain) N Quantum Wells by Visualization of Hot Carriers in Photoluminescence. *Appl. Phys. Lett.* **2013**, *103*, 071108.
(52) Kim, M.-H.; Schubert, M. F.; Dai, Q.; Kim, J. K.; Schubert, E. F.; Piprek, J.; Park, Y. Origin of Efficiency Droop in GaN-Based Light-Emitting Diodes. *Appl. Phys. Lett.* **2007**, *91*, 183507.
(53) Meyaard, D. S.; Lin, G.-B.; Cho, J.; Schubert, E. F.; Shim, H.; Han, S.-H.; Kim, M.-H.; Sone, C.; Kim, Y. S. Identifying the Cause of the Efficiency Droop in GaInN Light-Emitting Diodes by Correlating the Onset of High Injection with the Onset of the Efficiency Droop. *Appl. Phys. Lett.* **2013**, *102*, 251114.
(54) Hader, J.; Moloney, J.; Koch, S. Density-Activated Defect Recombination as a Possible Explanation for the Efficiency Droop in GaN-Based Diodes. *J. Appl. Phys.* **2010**, *96*, 221106.
(55) Hammersley, S.; Watson-Parris, D.; Dawson, P.; Godfrey, M.; Badcock, T.; Kappers, M.; McAleese, C.; Oliver, R.; Humphreys, C. The Consequences of High Injected Carrier Densities on Carrier Localization and Efficiency Droop in InGaN/GaN Quantum Well Structures. *J. Appl. Phys.* **2012**, *111*, 083512.
(56) Modine, N. A.; Armstrong, A. M.; Crawford, M. H.; Chow, W. W. Highly Nonlinear Defect-Induced Carrier Recombination Rates in Semiconductors. *J. Appl. Phys.* **2013**, *114*, 144502.
(57) Dai, Q.; Shan, Q.; Cho, J.; Schubert, E. F.; Crawford, M. H.; Koleske, D. D.; Kim, M.-H.; Park, Y. On the Symmetry of Efficiency-Versus-Carrier-Concentration Curves in GaInN/GaN Light-Emitting Diodes and Relation to Droop-Causing Mechanisms. *Appl. Phys. Lett.* **2011**, *98*, 033506.
(58) Lin, G.-B.; Shan, Q.; Birkel, A. J.; Cho, J.; Schubert, E. F.; Crawford, M. H.; Westlake, K. R.; Koleske, D. D. Method for Determining the Radiative Efficiency of GaInN Quantum Wells Based on the Width of Efficiency-Versus-Carrier-Concentration Curve. *Appl. Phys. Lett.* **2012**, *101*, 241104.
(59) Chow, W. W.; Crawford, M. H.; Tsao, J. Y.; Kneissl, M. Internal Efficiency of InGaN Light-Emitting Diodes: Beyond a Quasiequilibrium Model. *Appl. Phys. Lett.* **2010**, *97*, 121105.
(60) Chow, W. W. Modeling of Temperature and Excitation Dependences of Efficiency in an InGaN Light-Emitting Diode. *Opt. Express* **2014**, *22*, 1413−1425.
(61) Zhu, D.; Schubert, M. F.; Cho, J.; Schubert, E. F.; Crawford, M. H.; Koleske, D. D.; Shim, H.; Sone, C. Genetic Algorithm for Innovative Device Designs in High-Efficiency III-V Nitride Light-Emitting Diodes. *Appl. Phys. Express* **2012**, *5*, 012102.
(62) Zhu, D.; Noemaun, A. N.; Schubert, M. F.; Cho, J.; Schubert, E. F.; Crawford, M. H.; Koleske, D. D. Enhanced Electron Capture and Symmetrized Carrier Distribution in GaInN Light-Emitting Diodes Having Tailored Barrier Doping. *Appl. Phys. Lett.* **2010**, *96*, 121110.
(63) Crosslight Software. www.crosslight.com (accessed April 30, 2014).
(64) Lin, G.-B.; Meyaard, D.; Cho, J.; Schubert, E. F.; Shim, H.; Sone, C. Analytic Model for the Efficiency Droop in Semiconductors with Asymmetric Carrier-Transport Properties Based on Drift-Induced Reduction of Injection Efficiency. *Appl. Phys. Lett.* **2012**, *100*, 161106.
(65) Shim, J.-I.; Han, D.-P.; Kim, H.; Shin, D.-S.; Lin, G.-B.; Meyaard, D. S.; Shan, Q.; Cho, J.; Schubert, E. F.; Shim, H.; et al. Efficiency Droop in AlGaInP and GaInN Light-Emitting Diodes. *Appl. Phys. Lett.* **2012**, *100*, 111106.
(66) Chantre, A.; Vincent, G.; Bois, D. Deep-Level Optical Spectroscopy in GaAs. *Phys. Rev. B* **1981**, *23*, 5335.
(67) Passler, R. Photoionization Cross-Section Analysis for a Deep Trap Contributing to Current Collapse in GaN Field-Effect Transistors. *J. Appl. Phys.* **2004**, *96*, 715−722.
(68) Armstrong, A.; Crawford, M. H.; Koleske, D. D. Contribution of Deep-Level Defects to Decreasing Radiative Efficiency of InGaN/GaN Quantum Wells with Increasing Emission Wavelength. *Appl. Phys. Express* **2014**, *7*, 032101.
(69) Hierro, A.; Kwon, D.; Ringel, S.; Hansen, M.; Speck, J.; Mishra, U.; DenBaars, S. Optically and Thermally Detected Deep Levels in N-Type Schottky and P±N GaN Diodes. *Appl. Phys. Lett.* **2000**, *76*, 3064−3066.
(70) Armstrong, A.; Poblenz, C.; Green, D.; Mishra, U.; Speck, J.; Ringel, S. Impact of Substrate Temperature on the Incorporation of Carbon-Related Defects and Mechanism for Semi-Insulating Behavior in GaN Grown by Molecular Beam Epitaxy. *Appl. Phys. Lett.* **2006**, *88*, 082114.
(71) Seager, C.; Wright, A.; Yu, J.; Gotz, W. Role of Carbon in GaN. *J. Appl. Phys.* **2002**, *92*, 6553−6560.
(72) Armstrong, A.; Henry, T. A.; Koleske, D. D.; Crawford, M. H.; Lee, S. R. Quantitative and Depth-Resolved Deep Level Defect Distributions in InGaN/GaN Light Emitting Diodes. *Opt. Express* **2012**, *20*, A812−A821.
(73) Petroff, P.; Miller, R.; Gossard, A.; Wiegmann, W. Impurity Trapping, Interface Structure, and Luminescence of GaAs Quantum Wells Grown by Molecular Beam Epitaxy. *Appl. Phys. Lett.* **1984**, *44*, 217−219.
(74) Akasaka, T.; Gotoh, H.; Saito, T.; Makimoto, T. High Luminescent Efficiency of InGaN Multiple Quantum Wells Grown on InGaN Underlying Layers. *Appl. Phys. Lett.* **2004**, *85*, 3089−3091.
(75) Shockley, W.; Read, W., Jr. Statistics of the Recombinations of Holes and Electrons. *Phys. Rev.* **1952**, *87*, 835.
(76) Hall, R. Germanium Rectifier Characteristics. *Phys. Rev.* **1951**, *83*, 228.
(77) Sah, C.-T.; Shockley, W. Electron-Hole Recombination Statistics in Semiconductors Through Flaws with Many Charge Conditions. *Phys. Rev.* **1958**, *109*, 1103.
(78) Lang, D.; Henry, C. Nonradiative Recombination at Deep Levels in GaAs and Gap by Lattice-Relaxation Multiphonon Emission. *Phys. Rev. Lett.* **1975**, *35*, 1525−1528.
(79) Henry, C.; Lang, D. V. Nonradiative Capture and Recombination by Multiphonon Emission in GaAs and Gap. *Phys. Rev. B* **1977**, *15*, 989.
(80) Purcell, E. M. Spontaneous Emission Probabilities at Radio Frequencies. *Phys. Rev.* **1946**, *69*, 681−681.
(81) Boroditsky, M.; Vrijen, R.; Krauss, T. F.; Coccioli, R.; Bhat, R.; Yablonovitch, E. Spontaneous Emission Extraction and Purcell Enhancement from Thin-Film 2-D Photonic Crystals. *J. Lightwave Technol.* **1999**, *17*, 2096−2112.
(82) Noda, S.; Fujita, M.; Asano, T. Spontaneous-Emission Control by Photonic Crystals and Nanocavities. *Nat. Photonics* **2007**, *1*, 449−458.
(83) Russell, K. J.; Liu, T.-L.; Cui, S.; Hu, E. L. Large Spontaneous Emission Enhancement in Plasmonic Nanocavities. *Nat. Photonics* **2012**, *6*, 459−462.
(84) Sorger, V. J.; Pholchai, N.; Cubukcu, E.; Oulton, R. F.; Kolchin, P.; Borschel, C.; Gnauck, M.; Ronning, C.; Zhang, X. Strongly Enhanced Molecular Fluorescence Inside a Nanoscale Waveguide Gap. *Nano Lett.* **2011**, *11*, 4907−4911.
(85) Cho, C.-H.; Aspetti, C. O.; Turk, M. E.; Kikkawa, J. M.; Nam, S.-W.; Agarwal, R. Tailoring Hot-Exciton Emission and Lifetimes in Semiconducting Nanowires Via Whispering-Gallery Nanocavity Plasmons. *Nat. Mater.* **2011**, *10*, 669−675.
(86) Lakowicz, J. R.; Ray, K.; Chowdhury, M.; Szmacinski, H.; Fu, Y.; Zhang, J.; Nowaczyk, K. Plasmon-Controlled Fluorescence: A New Paradigm in Fluorescence Spectroscopy. *Analyst* **2008**, *133*, 1308−1346.

(87) Subramania, G.; Lee, Y.-J.; Fischer, A. J. Silicon-Based Near-Visible Logpile Photonic Crystal. *Adv. Mater.* **2010**, *22*, 4180.
(88) Subramania, G.; Li, Q.; Lee, Y.-J.; Figiel, J. J.; Wang, G. T.; Fischer, A. J. Gallium Nitride Based Logpile Photonic Crystals. *Nano Lett.* **2011**, *11*, 4591−4596.
(89) Miao, X.; Brener, I.; Luk, T. S. Nanocomposite Plasmonic Fluorescence Emitters with Core/Shell Configurations. *J. Opt. Soc. Am. B* **2010**, *27*, 1561−1570.
(90) Wierer, J. J.; Tsao, J. Y.; Sizov, D. S. Comparison Between Blue Lasers and Light-Emitting Diodes for Future Solid-State Lighting. *Laser Photonics Rev.* **2013**, *7*, 963−993.
(91) Huang, M. H.; Mao, S.; Feick, H.; Yan, H.; Wu, Y.; Kind, H.; Weber, E.; Russo, R.; Yang, P. Room-Temperature Ultraviolet Nanowire Nanolasers. *Science* **2001**, *292*, 1897−1899.
(92) Arafin, S.; Liu, X.; Mi, Z. Review of Recent Progress of III-Nitride Nanowire Lasers. *NANOP* **2013**, *7*, 074599−074599.
(93) Ma, Y.; Guo, X.; Wu, X.; Dai, L.; Tong, L. Semiconductor Nanowire Lasers. *Adv. Opt. Photon.* **2013**, *5*, 216−273.
(94) Lu, Y.-J.; Kim, J.; Chen, H.-Y.; Wu, C.; Dabidian, N.; Sanders, C. E.; Wang, C.-Y.; Lu, M.-Y.; Li, B.-H.; Qiu, X.; et al. Plasmonic Nanolaser Using Epitaxially Grown Silver Film. *Science* **2012**, *337*, 450−453.
(95) Oulton, R. F.; Sorger, V. J.; Zentgraf, T.; Ma, R.-M.; Gladden, C.; Dai, L.; Bartal, G.; Zhang, X. Plasmon Lasers at Deep Subwavelength Scale. *Nature* **2009**, *461*, 629−632.
(96) Kouno, T.; Kishino, K.; Yamano, K.; Kikuchi, A. Two-Dimensional Light Confinement in Periodic InGaN/GaN Nano-column Arrays and Optically Pumped Blue Stimulated Emission. *Opt. Express* **2009**, *17*, 20440−20447.
(97) Scofield, A. C.; Kim, S.-H.; Shapiro, J. N.; Lin, A.; Liang, B.; Scherer, A.; Huffaker, D. L. Bottom-up Photonic Crystal Lasers. *Nano Lett.* **2011**, *11*, 5387−5390.
(98) Xu, H.; Wright, J. B.; Luk, T.-S.; Figiel, J. J.; Cross, K.; Lester, L. F.; Balakrishnan, G.; Wang, G. T.; Brener, I.; Li, Q. Single-Mode Lasing of GaN Nanowire-Pairs. *Appl. Phys. Lett.* **2012**, *101*, 113106.
(99) Xu, H.; Wright, J. B.; Hurtado, A.; Li, Q.; Luk, T.-S.; Figiel, J. J.; Cross, K.; Balakrishnan, G.; Lester, L. F.; Brener, I.; et al. Gold Substrate-Induced Single-Mode Lasing of GaN Nanowires. *Appl. Phys. Lett.* **2012**, *101*, 221114.
(100) Wright, J. B.; Liu, S.; Wang, G. T.; Li, Q. M.; Benz, A.; Koleske, D. D.; Lu, P.; Xu, H. W.; Lester, L.; Luk, T. S.; et al. Multi-Colour Nanowire Photonic Crystal Laser Pixels. *Sci. Rep.* **2013**, *3*, 2982.